POLITECNICO DI TORINO
Repository ISTITUZIONALE

CFD analysis of a regular sector of the ITER vacuum vessel. Part II: Thermal-hydraulic effects of the nuclear heat load

Original
CFD analysis of a regular sector of the ITER vacuum vessel. Part II: Thermal-hydraulic effects of the nuclear heat load / Zanino, Roberto; Savoldi, Laura; Subba, Fabio; Corpino, Sabrina; Izquierdo, J.; Le Barbier, R.; Utin, Y.. - In: FUSION ENGINEERING AND DESIGN. - ISSN 0920-3796. - 88:(2013), pp. 3248-3262. [10.1016/j.fusengdes.2013.10.005]

Availability:
This version is available at: 11583/2521896 since:

Publisher:
ELSEVIER

Published
DOI:10.1016/j.fusengdes.2013.10.005

Terms of use:

This article is made available under terms and conditions as specified in the corresponding bibliographic description in the repository

Publisher copyright

(Article begins on next page)

18 April 2024

CFD analysis of a regular sector of the ITER vacuum vessel. Part II: Thermal-hydraulic effects of the nuclear heat load

R. Zanino [a,*], L. Savoldi Richard [b], F. Subba [c], S. Corpino [b], J. Izquierdo [c], R. Le Barbier [d], Y. Utin [d]

[a] *Dipartimento Energia, Politecnico di Torino, 10129 Torino, Italy*
[b] *Dipartimento di Ingegneria Meccanica e Aerospaziale, Politecnico di Torino, 10129 Torino, Italy*
[c] *F4E, Barcelona, Spain*
[d] *ITER IO, Cadarache, France*

A B S T R A C T

The 3D Computational Fluid Dynamic (CFD) steady state analysis of the regular sector #5 of the ITER vacuum vessel (VV) is presented in these two companion papers using the commercial software ANSYS-FLUENT®. The pure hydraulic analysis, concentrating on flow field and pressure drop, is presented in Part I. This Part II focuses on the thermal-hydraulic analysis of the effects of the nuclear heat load. Being the VV classified as safety important component, an accurate thermal-hydraulic analysis is mandatory to assess the capability of the water coolant to adequately remove the nuclear heat load on the VV. Based on the recent re-evaluation of the nuclear heat load, the steady state conjugate heat transfer problem is solved in both the solid and fluid domains. Hot spots turn out to be located on the surface of the inter-modular keys and blanket support housings, with the computed peak temperature in the sector reaching ~290 °C. The computed temperature of the wetted surfaces is well below the coolant saturation temperature and the temperature increase of the water coolant at the outlet of the sector is of only a few °C. In the high nuclear heat load regions the computed heat transfer coefficient typically stays above the 500 W/m^2 K target.

1. Introduction

The ITER vacuum vessel (VV) will be located inside the cryostat and it will house the in-vessel components, providing a high quality vacuum for the plasma and the first confinement barrier [1,2]. The VV is a double-wall structure where the volume between the inner and outer shells is designed to allow the circulation of the cooling water through a complicated structure including the in-wall shielding (IWS) made of borated stainless steel plates.

The VV is partitioned in 9 sectors, each occupying 40°, with three bands of ports located on the outboard side. Each sector is actively cooled by pressurized sub-cooled water at 100 °C and 0.9 MPa, entering from dedicated piping on the lower port, bifurcating and flowing both in the inboard and in the outboard side through the space left open between inner and outer shell as well as in other auxiliary structures, see below, before joining again and being routed through the upper port frame to an exit pipe. Here only half (20°) of the sector will be considered, see Fig. 1, assuming symmetry around the poloidal plane bisecting the central equatorial port.

In Part I of this paper [3], we presented a detailed *hydraulic* analysis of the VV RS #5, considering only the fluid portion of the domain and ignoring the thermal load of nuclear origin which acts on the VV during the operation of the machine. Here we address the steady-state conjugate heat transfer problem, including the VV solid structure and concentrating on the thermal-hydraulic effects of the recently re-calculated nuclear heat load.

As discussed in [3], previous published CFD work on the ITER VV [4,5], was based on the design status in 2006 and did not include several of the important features of the VV like the Inter-Modular Keys (IMKs), the Blanket Support Housings (BSHs) or the Triangular Support (TrS).

2. Model

As in [3], the Reynolds-Averaged Navier–Stokes (RANS) model with SST k-ω [6] turbulence closure was chosen to compute the steady-state flow field in the VV. Now the energy equation is also solved, both in the water coolant and in the solid structures, determining the temperature distribution in the two sub-domains. The

* Corresponding author.
E-mail address: roberto.zanino@polito.it (R. Zanino).

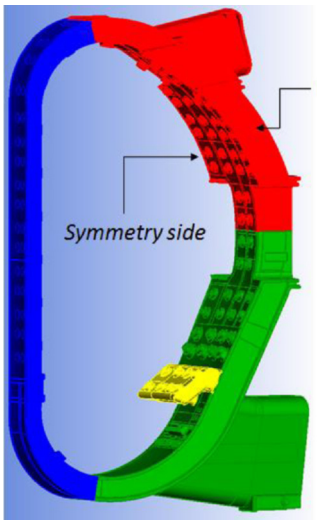

Fig. 1. Schematic view of (half) of the VV regular sector #5, ~11.5 m tall. The three segments constituting the sector are highlighted: inboard (Inb) in blue, outboard bottom (OB) with the lower port and the two half equatorial ports in green, outboard top (OT) with the two half equatorial ports and the upper port in red. The triangular support (TrS) is also shown, in yellow. The original 40° sector is bisected leaving a "symmetry side". On the side facing the reader the field joints (FJ) are located, connecting this sector to the neighbouring sector. (For interpretation of the references to colour in this figure legend, the reader is referred to the web version of this article.)

energy balance of the coolant is coupled to the flow field through the advective contribution to the energy flux, while the thermal coupling between fluid and structures is achieved by enforcing the continuity of temperature and heat flux at the interface (wall). Therefore, the heat transfer coefficient (HTC) between coolant and wall is an output (not an input) of our calculation. Finally, the temperature feeds back on the flow field both through the effect of buoyancy and through temperature-dependent thermo-physical properties.

The software packages adopted for the present analysis are the same as in [3], except a more recent version of ANSYS ICEM [7], 14.5, was used for the smoothing of the grids.

3. Computational solid domain

The RS #5 can be divided into different segments, see Fig. 1, including the inboard (Inb) segment, the two outboard, bottom (OB) and top (OT) segments, and the Triangular Support (TrS) structure.

The solid domain retained for the thermal-hydraulic analysis can be split in two parts: the IWS and the rest, which will be called "skeleton" below. The IWS and the skeleton domains are shown in Figs. 2 and 3 for the case of the Inb and OT segment, respectively. The TrS solid domain is shown in Fig. 4.

In Fig. 2a, the location of the toroidal ribs, which constitute as seen in [3] an obstacle for the fluid flow in the Inb segment, is clearly visible, while in Fig. 2b several details of the skeleton included in our modelling (like divertor rails, IMKs, BSHs and centering keys) are highlighted. In Fig. 3a, the space left empty for the internal poloidal ribs is highlighted together with IMK #9.

For the TrS, no IWS is foreseen in the cavity occupied by the fluid. As opposed to the rest of the VV skeleton, which is made of stainless steel, the TrS is made also of copper, as shown in Fig. 4.

4. Mesh generation in the solids

The mesh is generated by ICEM using the Octree algorithm. As in the case of the fluid domain, the mesh was separately generated

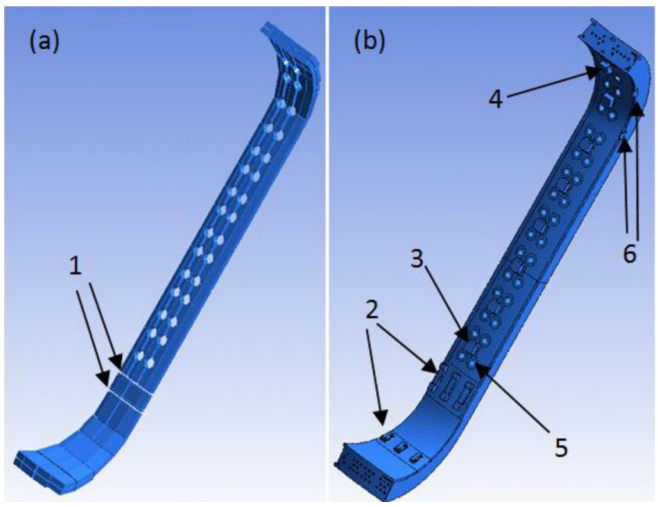

Fig. 2. Inb solid domain: (a) IWS, with empty space left by the toroidal ribs (marked with "1"). (b) Skeleton with divertor rails (marked with "2"), IMKs #1 (marked with "3") to #8 (marked with "4"), blanket support housings (marked with "5") and centering keys (marked with "6").

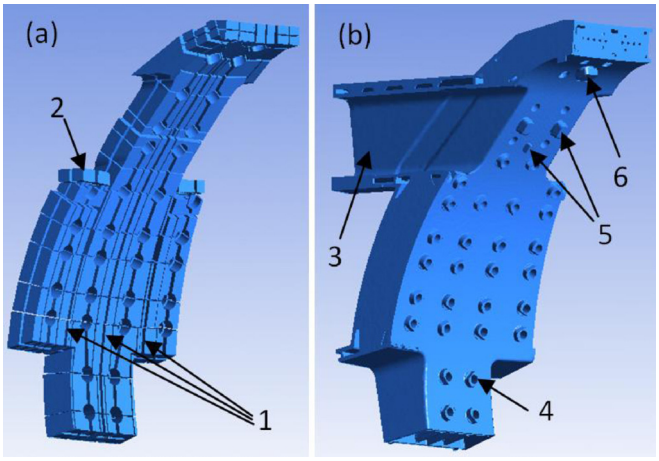

Fig. 3. OT solid domain: (a) IWS, with empty space left by the poloidal ribs (marked with 1), including horizontal tiles below the upper port (marked with "2″). (b) Skele-ton with upper port (marked with 3), blanket support housings (marked with 4), centering keys (marked with 5) and the IMK #9 (marked with 6).

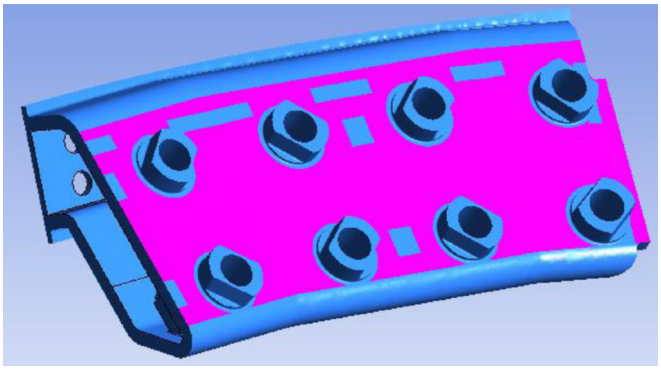

Fig. 4. TrS solid domain (stainless steel in blue, copper plates in pink). (For interpretation of the references to colour in this figure legend, the reader is referred to the web version of this article.)

Table 1
Solid mesh features.

Segment	Part	# of MCells
OB	Skeleton	6.37
	IWS	6.07
OT	Skeleton	7.27
	IWS	5.44
Inb	Skeleton	4.26
	IWS	3.53
TrS	Skeleton (SS)	5.11
	Plates (Cu)	0.13
	Total	38.18

in each of the three segments (and in the TrS). The mesh of the solid domain is made of tetrahedra and the number of cells in the differ-ent portions of the domain is reported in Table 1. Added to the cells in the fluid domain these ∼40 million cells would give a total mesh size for the thermal-hydraulic (conjugate heat transfer) problem of

∼90 million cells. A strategy to reduce the computational effort has been therefore developed consisting in splitting the global problem into suitably coupled sub-problems.

The computational domains in the three segments and in the TrS have been meshed separately, for the sake of simplicity, considering for each segment the solid and the fluid domain simultaneously. The maximum global element seed size was set to 256 mm (64 mm for the TrS), the minimum element size for proximity/curvature-based refinement was set to 8 mm, the maximum grid size of 16 mm was adopted on the walls (except in the TrS, where a finer mesh was required). A global scaling parameter of 1.15 has been then adopted for all the tetrahedra.

Figs. 5 and 6 shows some details of the mesh developed for the thermal-hydraulic simulations presented in this paper. Fig. 5 shows a cross section of the Inb segment, where the two different parts of the solid domain are highlighted (skeleton in red, IWS in yellow) together with the fluid domain (in light blue). Fig. 6 shows some important details of the skeleton protruding towards the plasma from different segments of the inner shell and, as such, particularly

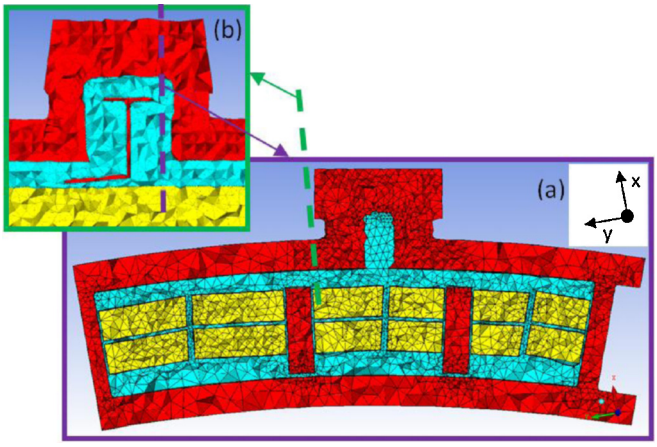

Fig. 5. (a) Detail of the mesh on a cross section of the Inb segment on a plane parallel to the equatorial plane and cutting the IMK #4. (b) Detail of the mesh on a cross section of an IMK on a plane across *y* showing the flow driver.

relevant for the thermal-hydraulic analysis as possible locations of temperature hot spots.

As in the case of the fluid domain [3], also the generation of the mesh in the solid domain was a quite complex problem, due mostly to the large number of small details in a comparatively large compu-tational domain. As a consequence, the first grid created with ICEM was never fully satisfactory and several smoothing steps proved to be necessary, see Appendix A.

5. Nuclear heat load

During plasma operation, the heat produced by nuclear reactions will be deposited into the first wall and the VV structure. The level of heat deposition can be differentiated depending on the region involved. This is observed in neutronics analysis consist-ing in Monte Carlo transport simulations, from which inputs to the thermal-hydraulics are derived. The reference neutronics analysis

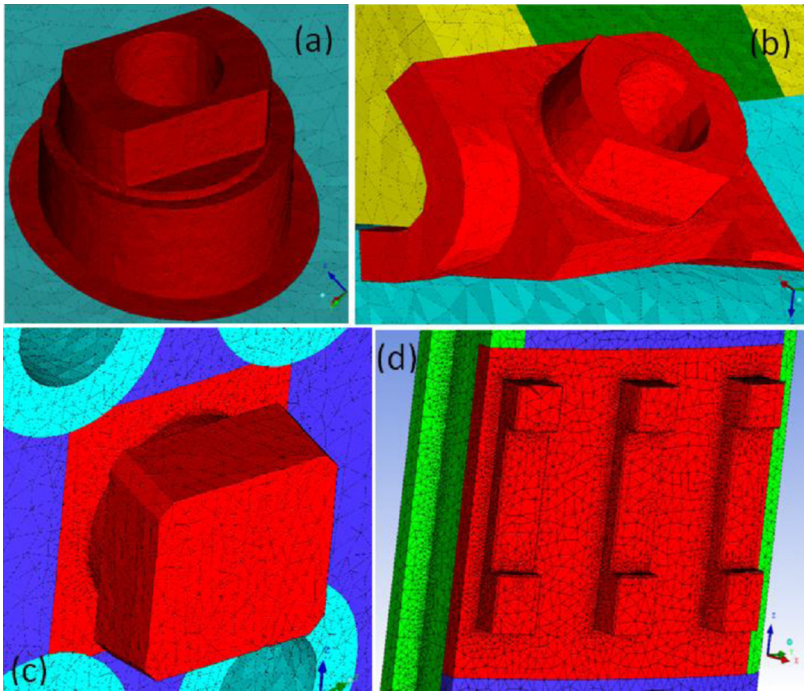

Fig. 6. Details of the mesh in the solid: (a) Housing in the OB segment; (b) housing on the upper port frame in the OT segment; (c) IMK and (d) divertor rail in the Inb segment.

were performed on the so-called B-Lite model, including a 40° sector of VV, blanket, divertor, thermal shield and magnets, and based on the FENDL 2.1 nuclear data. Considering the size and complexity of the geometry, the heating outputs of the neutronic analysis have been integrated on the following sub-domains and then derived as volumetric heating values for the need of the thermal-hydraulics:

1. Inner shell, assumed to extend 6 cm deep in the VV skeleton from its plasma-side surface.
2. IWS, poloidal and Toroidal ribs, blanket support housings (all steel structures between the 2 VV shells).
3. Outer shell, assumed to extend 6 cm deep in the VV skeleton, going inwards from its outer surface.
4. Lower, equatorial and upper ports, which include the port stub and a part of the port stub extension.
5. IMKs.

The heat generated in the inner shell, IWS and outer shell i.e. the first three regions in the list above, is defined by a poloidal distribution with ~6° resolution. For each port as well as for each IMK, it assumes a constant value, see Fig. 7. This distribution is more accurate than what was used in [1,8], where the estimated nuclear heat load was lower and a purely radial distribution with exponential decay was adopted.

The heat deposition in the water is applied on the IWS only, except in the TrS, which mainly contains water.

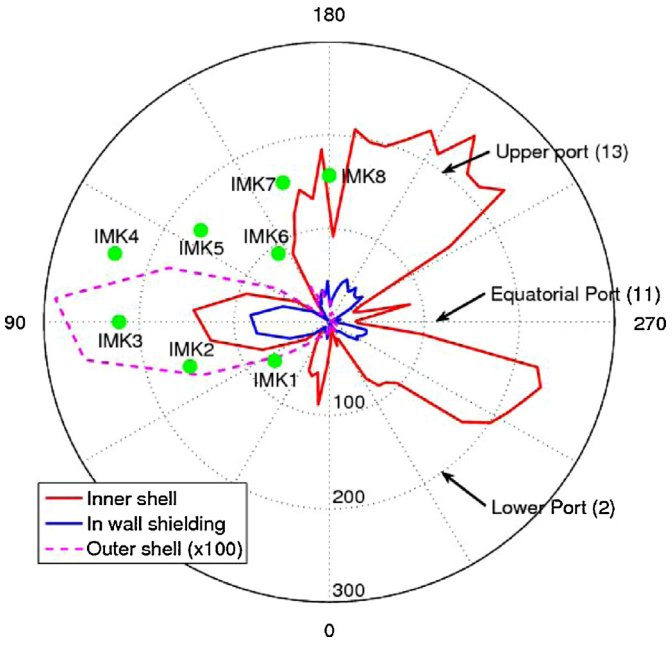

Fig. 7. Polar plot of the nuclear heating [kW/m^3] in the different components of the VV model. Notice that the load on the outer shell has been magnified ×100 to make it visible on the same scale.

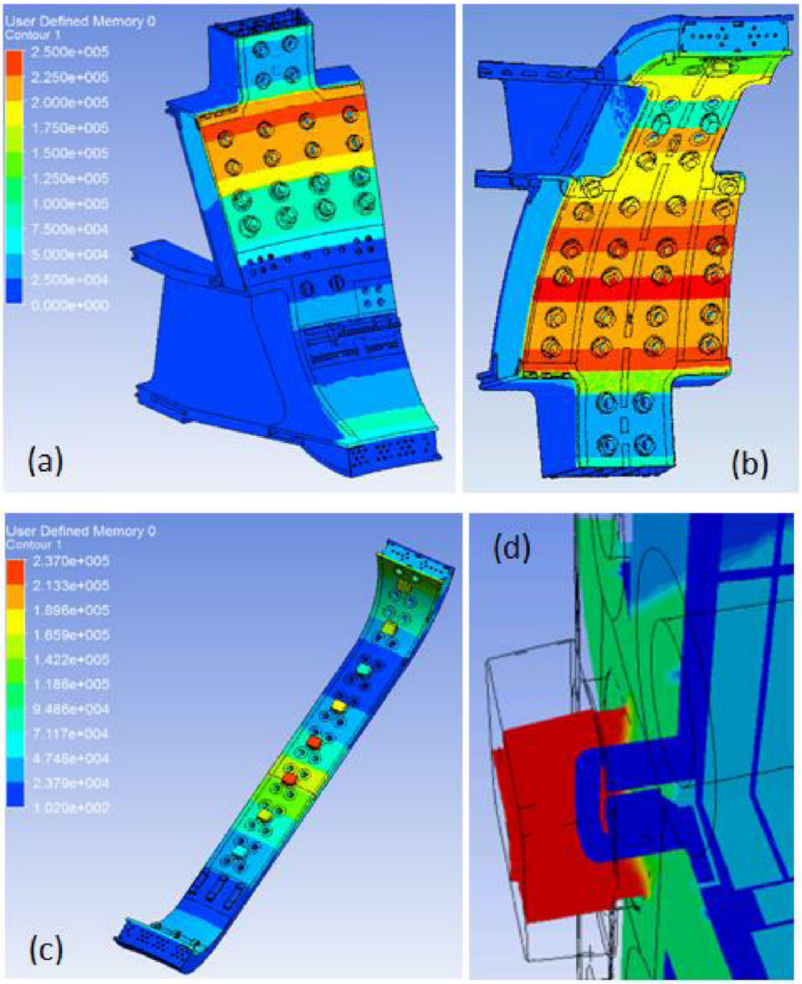

Fig. 8. Distribution of the volumetric nuclear heat load (W/m^3) on the solid domain of: (a) OB segment, (b) OT segment, (c) Inb segment, and (d) detail of IMK4.

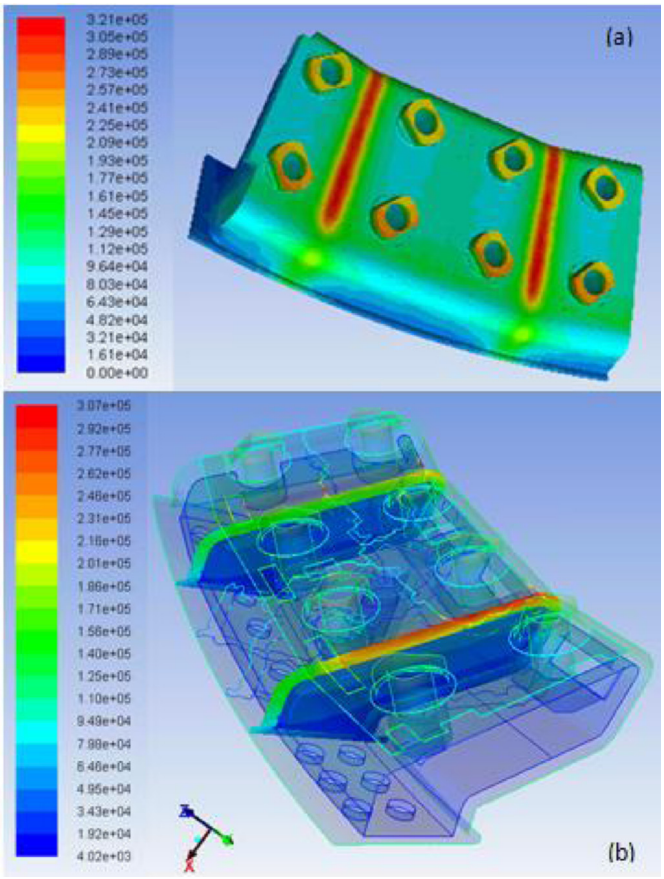

Fig. 9. Distribution of the volumetric nuclear heat load (W/m^3) on the TrS: (a) solid domain and (b) fluid domain.

Fig. 7 shows the distribution of the nuclear heat load on the inner shell, outer shell, IWS, ports and IMK. In the polar plot, the left semi-circle represents the Inb segment, while the equatorial plane is represented by the horizontal diameter. It is seen that the largest load occurs on the inner shell of the OT segment, as well as just below the equatorial port in the OB. The most loaded IMK results to be the #4, in the Inb segment.

The maps of the nuclear heat load in the OB, OT, Inb segments, and on the most loaded IMK4, are reported in Fig. 8, clearly showing the poloidal distribution of the load. Fig. 9a and b shows the nuclear heat load in the solid and fluid domains of the TrS, respectively

6. Simulation setup and strategy

The thermal-hydraulic simulation was performed separately for the different segments of the VV (Inb, OB, OT, TrS), relying on the mass flow rate distribution computed in the hydraulic simulation. The global consistency of the results is verified a posteriori, see below.

We use the SIMPLE scheme for the pressure-velocity coupling, with first order upwind spatial scheme for momentum, turbulent kinetic energy, turbulent dissipation rate and energy equations. The segregated approach is adopted. The runs have been performed without under-relaxation of the energy equation, while for the other equations the same strategy adopted for the hydraulic simulation [3] was followed here.

In all cases, a preliminary hydraulic simulation has been run, and only after a stable flow field has been computed, the energy equation has been switched on.

6.1. Material properties

Since we expect the nuclear heat load to cause a non-negligible temperature increase in the VV, we adopt temperature dependent material properties (specific heat and thermal conductivity) for both the solid materials (SS and Cu), see Appendix B, and for the water coolant (including, besides specific heat and thermal conductivity, also density and viscosity) [9,10].

6.2. Boundary conditions

The conductive and radiative heat flux is assumed to vanish on the surface of the sector, which is therefore considered adiabatic except for the advective inlet and outlet contributions of the water coolant, on which we concentrate on the rest of this section.

In the global problem of the VV (half) sector, the boundary conditions related to the advective contribution are: mass flow rate = 41.45 kg/s and temperature = 100 °C at the first section of the inlet pipe to the lower port, “outflow” boundary condition at the final section of the outlet pipe from the upper port. The “outflow” boundary condition forces the weak constraint that, for a prescribed fraction of the mass flow rate entering the computational domain (100% in this case), the flow is fully developed (zero gradient of the velocity field in the direction perpendicular to the surface).

Here, in order to make the size of the thermal-hydraulic problem computationally more tractable, we separately compute the solution on each segment, then iteratively find a global solution. This approach requires in turn specifying boundary conditions for each segment, including the interfaces between the different segments. While the conductive flux is assumed to be negligible at these interfaces, for the advective fluxes we need two informations: (1) the mass flow rate through each inflow and outflow portion of any interface; (2) the inlet temperature to each inflow portion of the interface.

As to the first item, we rely on (and keep frozen for the entire pro-cedure) the mass flow rate distribution computed in the hydraulic simulation presented in the companion paper [3]. The mass flow rate computed through the different permeable portions of the interface between different segments (e.g., through the holes in the connection plates between OB and Inb and/or Inb and OT) is used as boundary condition, if that portion of the interface is an inflow boundary for that segment, while for the other portions an “outflow” boundary condition is imposed. In order to assess the accuracy of the global solution, subject to the constraint of frozen mass flow rate distributions at the interface between different segments, a self-consistency check will be presented below in Section 7.2.

As to the second item, an iterative simulation strategy has been developed, for the identification of the fluid temperature at the interface between the different segments, to be used as boundary condition for any inflow portion of the boundary of that segment. Iterations are necessary because, for instance, the temperature of the water re-circulating back from the Inb to the OB, that is computed by the simulation of the Inb segment, is influenced by the temperature of the fluid entering the Inb from the OB itself, and the OB fluid temperature near the interface is influenced by the temperature of the fluid re-entering the OB from the Inb.

The following set of boundary conditions has been consistently adopted for the simulation of the different segments:

- OB – mass flow rate entering the inlet pipe, at the inlet temperature (100 °C); mass flow rate entering from the Inb and TrS, at the temperature resulting from the Inb and TrS simulations, respectively; “outflow” boundary condition for the outflow portions of the interface to the Inb, TrS and OT segments.

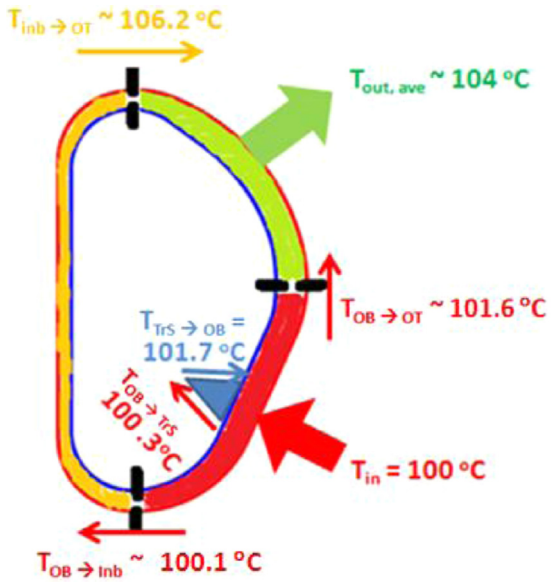

Fig. 10. Average temperature of the flow transferred at the interfaces between the different VV segments. The arrows indicate the direction of the net flow.

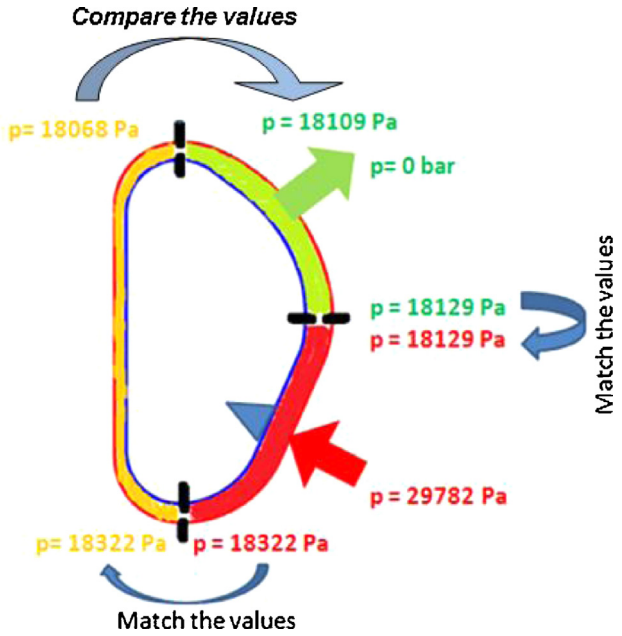

Fig. 11. Schematic view of the procedure and results of the self-consistency check of the thermal-hydraulic analysis of the different segments.

- TrS – mass flow rate entering from the OB, at the temperature computed in the OB simulation; "outflow" boundary condition for the outflow portions of the interface to the OB segment.
- Inb – mass flow rate entering from the OB and OT, at the temperature resulting from the OB and OT simulations, respectively; "outflow" boundary condition for the outflow portions of the interface to the OB and OT segments.
- OT – mass flow rate entering from the OB and Inb, at the temperature computed from the OB and Inb simulations, respectively; "outflow" boundary condition for the outflow portions of the interface to the Inb segment and for the outlet pipe.

The iterations are initialized at the global VV inlet temperature, and the temperature field is computed for the first time for each of the four segments; the computed outlet temperature at any interface is then used as inlet boundary condition for the adjacent segment in the second iteration. At the third iteration, the average absolute temperature difference between two successive iterations turned out to be ~0.01 °C, which we consider sufficiently small to stop the iterations.

The average water temperature (weighted with the respective mass flow rate) computed for the flow entering each segment is reported in Fig. 10. The computed outlet temperature results to be ~104 °C.

7. Results and discussion

The results of the simulation performed for each segment are presented in this section, first in terms of residuals, monitors and level of accuracy in the energy conservation. Then the check of the internal consistency of the simulation strategy is performed, before presenting and discussing the computed maps of the temperature and of the heat transfer coefficient.

7.1. Self-consistency check

Before proceeding with the detailed discussion of the simulation results, we must first observe that the strategy adopted in this Part II, which uses the output of the hydraulic simulation of Part I [3] as input for the thermal-hydraulic analysis, is not self-consistent, since the temperature effects included in the model will lead to a somewhat different flow and pressure field than computed in Part I.

The check of the self-consistency of our analysis is then performed by computing first the average pressure level at the interfaces between the different segments, post-processing the simulation of each segment. Since there is no dependence of the water material properties on the fluid pressure, the latter can be treated as a "potential", in the sense that an offset can be added or subtracted to the entire pressure field. We then proceed poloidally in the clockwise direction, starting from the OT/Inb interface, and check to what accuracy we are then able to recover the same pressure p(OT/Inb) after running along the entire VV as follows (see also Fig. 11):

- Considering as reference the pressure level computed in the OT segment, the offset between OT and OB on the average pressure computed at the interface between the two (outboard equatorial plane) is removed from the pressure field of the entire OB simulation;
- The resulting offset between OB and Inb on the average pressure computed on the connection grid between Inb and OB is removed from the pressure field of the entire Inb simulation;
- At this point, the two pressure levels resulting in the Inb and in the OT on the connection grid between Inb and OT (OT/Inb interface) are compared. The computed difference is ~16% of the total pressure drop on the Inb, see Fig. 11, which would lead to a maximum difference of 7–8% in the mass flow rate passing through the Inb, i.e. an absolute difference up to 0.3 kg/s. We consider this difference acceptably small in relative terms and confirming the accuracy of our results.

A similar check has been performed on the TrS, computing the pressure drop between the average inlet and outlet pressure both in the TrS and OB simulations. The two values differ by 4.3%, which we consider acceptable.

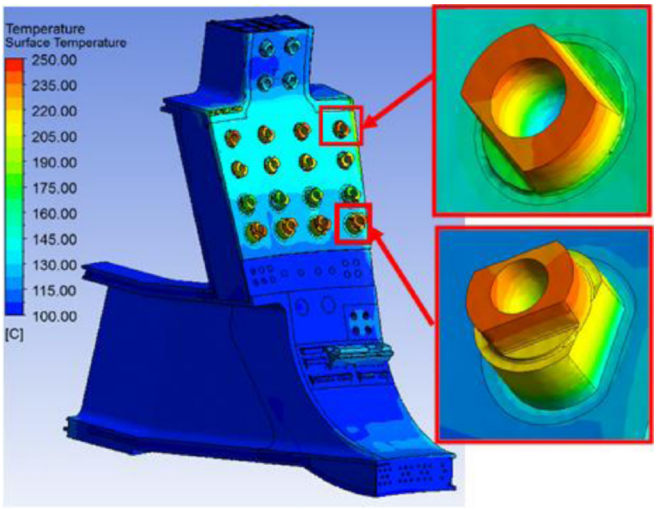

Fig. 12. Temperature map on the surface of the inner shell in the OB segment. In the insets: zoom on the hot spot regions.

7.2. Temperature field in the VV structure (non-wetted surfaces)

The computed temperature distribution in the VV structures is presented in this section, with particular reference to non-wetted surfaces. The temperature maps of the water coolant and of the wetted surfaces are presented in Sections 7.3 and 7.4, respectively.

In Fig. 12 we show the computed temperature map on the OB inner shell. As expected from the heat load maps, see Figs. 7 and 8, the shell is much hotter just below the equatorial port than at the level of the lower port. The first row of housings just below the equatorial ports contains then hot spots in view of the high load, see Fig. 7, while the housings on the fourth row are also hot spots, because of their distance from the cooling water (their height is much larger than that of the first row, see Fig. 8). The maximum temperature on the housings is ∼250 °C, thanks to the cooling chan-nel introduced into the housing body, while that of the inner shell does not exceed almost anywhere the 160 °C, which are the typical maximum temperatures estimated in previous simplified analyses [1,8].

The temperature map computed for the Inb is reported in Fig. 13. The effect of the poloidal distribution of the heat load is again clearly visible. The hot spots in this segment are located on the plasma facing surface of the IMKs, as shown in the insets. The maximum temperature reaches ∼230 °C on the IMK #4. The shell temperature remains below 140 °C everywhere.

The computed temperature map on the OT segment is reported in Fig. 14. As expected from the features highlighted in Fig. 7, the inner shell is much hotter in the OT than in the Inb segment, due to the larger nuclear heat load. The hot spots reach ∼290 °C, the highest temperature computed in the entire sector, and are located on the two housings on the upper port frame.

The hot spot temperatures computed in all segments are well above those estimated by simplified models in previous work, mainly as a consequence of the increased nuclear load and its detailed distribution, as well as of the fact that important details of the VV structure, like housings and keys, have been included here in the computational model for the first time.

On the other hand, the temperature increase in the IWS is limited everywhere to few degrees (not shown), in view of the relatively low nuclear load. This also offers a further justification of the simplification of the IWS structure discussed in [3], as the IWS is not a critical component from the thermal point of view.

The temperature map on the plasma side of the TrS, presented in Fig. 15, is rather asymmetric since an SS wall is present on the right, while a symmetry boundary condition is adopted on the left side. This is the only place in the entire VV sector where a large fluid area is present, and thus the only place where a non-negligible asymmetry in the toroidal direction could be encountered. The TrS hot spots are located on the top surface of the rightmost housings, where a temperature of ∼230 °C is reached.

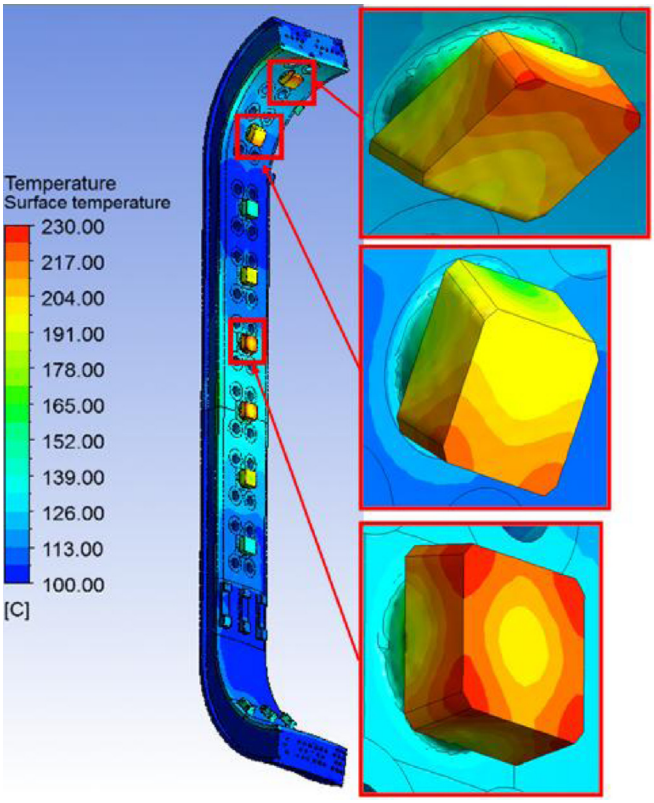

Fig. 13. Temperature map on the surface of the inner shell in the Inb segment. In the insets: zooms on the hottest IMKs.

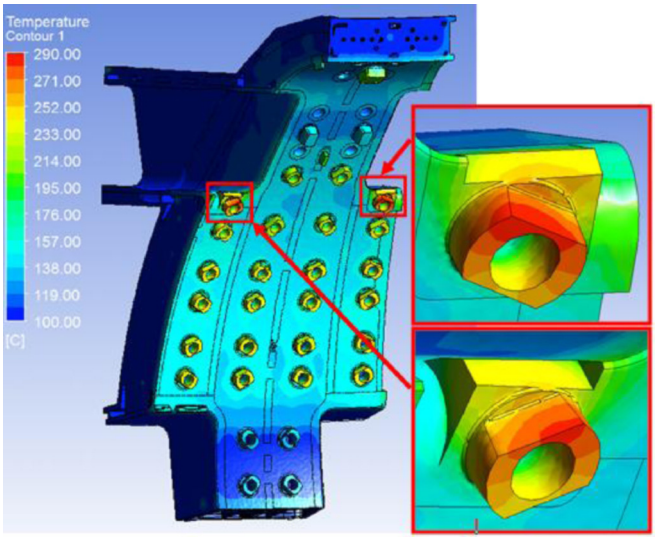

Fig. 14. Temperature map on the surface of the inner shell in the OT segment. In the insets: zoom on the hot spots, corresponding to the housings located on the frame of the upper ports.

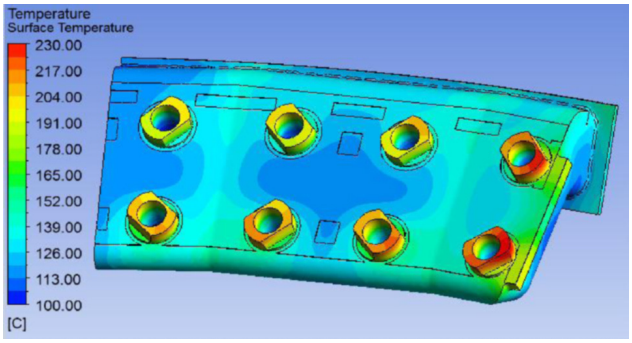

Fig. 15. Temperature map on the plasma-side surface of the TrS segment.

7.3. Coolant flow and temperature field

We report here the computed flow field of the coolant under the effect of the nuclear heat load, using pathlines coloured by the temperature level. This will integrate the discussion of Part I [3], where the flow field resulting from the sole constraint of the forced inlet mass flow rate was presented.

We consider first of all the OB, with particular reference to the fluid path in the four parallel poloidal channels in which the flow is split by the poloidal ribs. The flow arriving directly from the lower port contributes to the cooling of the portion of the VV just above the port itself, see Fig. 16. The cooling of the portion of the sector adjacent to the field joint is provided mainly by the fluid that re-enters the OB segment after recirculation from the Inb, see Fig. 16b.

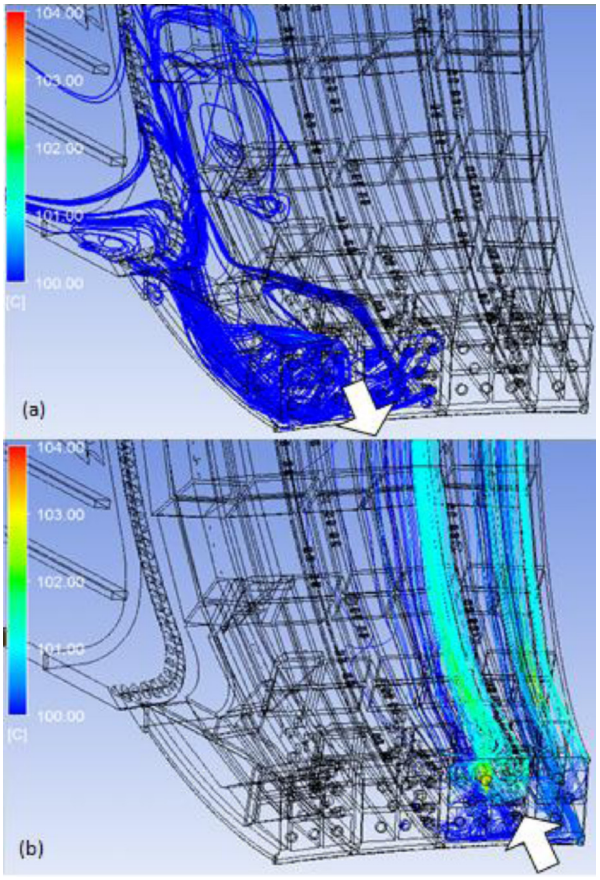

Fig. 16. Pathlines from the connection grid between OB and Inb, coloured by the fluid temperature: (a) drawn backwards and (b) drawn forward. (For interpretation of the references to colour in this figure legend, the reader is referred to the web version of this article.)

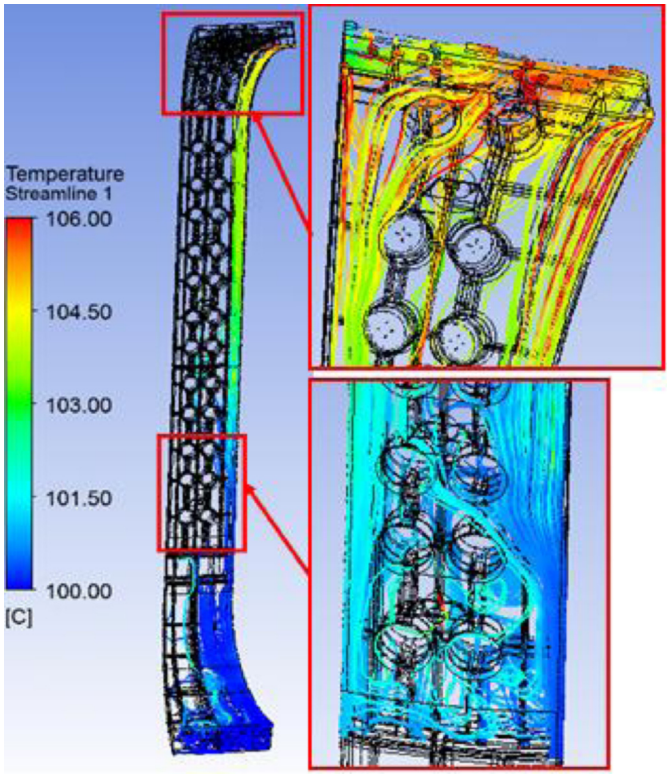

Fig. 17. Pathlines of the coolant in the gap adjacent to the inner shell in the OT, coloured by the fluid temperature and drawn forward from the Inb-OB connection plate. Zooms of the different regions are reported in the insets. (For interpretation of the references to colour in this figure legend, the reader is referred to the web version of this article.)

The two central poloidal channels of the OB segment are cooled mainly by the fluid exiting from the TrS, see also [3].

The flow distribution among the different poloidal channels of the OB is strongly non uniform, also close to the equatorial plane, where the two side channels show a lack of coolant with respect to the central ones (not shown). A further investigation of this aspect would be required to optimize the size and position of the few communication holes drilled in the poloidal ribs, in order to achieve a more uniform coolant flow distribution in the entire sector.

In Fig. 17 the pathlines of the coolant flow in the Inb segment are reported, showing as in the case of the OB a strong dependence on the location of the fluid inlet: indeed, the fluid tends to move straight upwards from the connection plate with the OB, see also [3], causing a large flow (and temperature) non-uniformity in the sector.

In Fig. 18 we show the interaction between flow and temperature field in the hottest IMK of the Inb. The role of the flow driver in forcing the fluid to flow close to the IMK head (hot spot) is captured by the simulation. The max coolant speed in the IMK is ~0.1 m/s.

The flow in the IMK is extremely sensitive to the nuclear heat load, see Fig. 19 where the solution in the presence of the nuclear heat load (left) is compared with the case of no nuclear heat load as computed in Part I (right). It is clear that the nuclear heat load causes a significant acceleration of the coolant flow in the chan-nel between inner shell and IWS, which feeds the IMK. This can be qualitatively justified as follows: the heat transferred from the inner shell (directly subject to the highest nuclear heat load, see Fig. 7) to the water coolant leads to a significant decrease of the viscosity as the temperature increases, while in the other main flow channel, between IWS and outer shell, the temperature and therefore the viscosity are basically unchanged, because of the much smaller nuclear heat load in IWS and outer shell, see Fig. 7. This

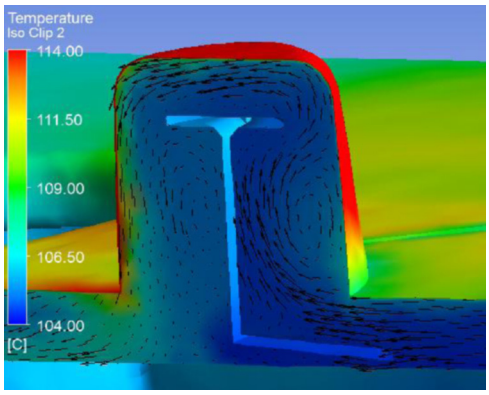

Fig. 18. Temperature map on a longitudinal cross section cutting the IMK #4. The flow field is also reported by black arrows, whose length is proportional to the veloc-ity magnitude. The temperature is not clipped to its largest value, i.e., the values larger than 114 °C are represented equal to 114 °C. (For interpretation of the refer-ences to colour in this figure legend, the reader is referred to the web version of this article.)

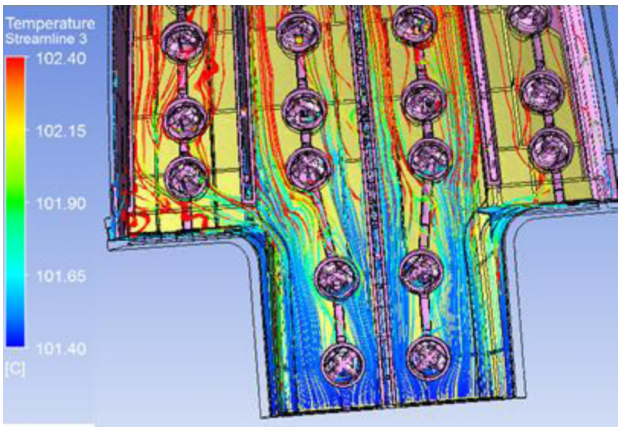

Fig. 20. Pathlines of the coolant in the gap adjacent to the inner shell in the OT, coloured by the fluid temperature and drawn forward from the equatorial plane. The IWS is shown in yellow. (For interpretation of the references to colour in this figure legend, the reader is referred to the web version of this article.)

asymmetry, causes a significant asymmetry in the change of the flow impedance due to nuclear heating in the two channels, which results in a significant change in the flow distribution. The struc-ture of the vortex generated downstream of the flow driver is also significantly affected, with faster reattachment at higher speed, i.e., when the nuclear heating is present.

The flow field in the OT and the corresponding heating of the coolant along the pathlines is shown in Fig. 20 with particular ref-erence to the gap adjacent to the inner shell. Some asymmetry in the fluid flow and corresponding cooling capability along the differ-ent poloidal cooling channels is noted. The flow from the restricted passage between the equatorial ports has more difficulty to reach the side towards the field joints (on the right in the figure) than the side towards the poloidal midplane, which corresponds to the location of the fluid inlet on the lower port.

The TrS constitutes, with respect to the rest of the VV, a some-what non-typical segment, since no IWS is present in the relatively large fluid volume. The temperature maps in a couple of poloidal cross sections of the TrS are presented in Fig. 21. The cooling water enters into the bottom region of the TrS (Fig. 21a), and it exits from the top region (see Fig. 21b) after a moderate temperature increase of ∼1.4 °C, see also Fig. 10. In order to allow an efficient cooling of all the parts of the TrS, a channel (visible in the bottom-left cor-ner of Fig. 21a) has been purposely drilled in the metal wall more exposed to the nuclear heat load. The fluid temperature increase is limited almost everywhere in the TrS, with the exception of the upper region, where a hot spot (temperature increase up to ∼7 °C) develops, adjacent to the plasma-side surface, in correspondence to a region of recirculating flow. Buoyancy effects are accounted for in the simulation of the flow field inside the TrS, but they were obviously not included in the purely hydraulic model of Part I, whose results were adopted to set the boundary conditions for each segment in this Part II. The consistency check, see Section 7.2, shows that this should not introduce a major difference.

7.4. Heat transfer between structures and coolant

In this section, we finally report on the derivation of the maps of the heat transfer coefficient (HTC) between water coolant and VV structures, starting from the post-processing of the computed results. In principle, the standard definition $HTC_{\mathrm{def}} = q''/(T_S - T_B)$ could be adopted. This requires the knowledge of the (local) heat flux q'' on the surface of the structures wetted by the coolant (referred to as "wall heat flux" in what follows), of the (local) surface

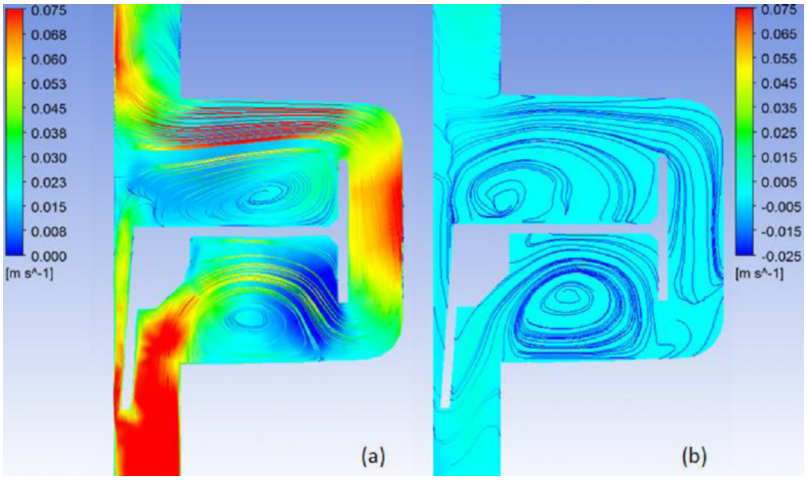

Fig. 19. Comparison between computed flow field in the IMK #4: (a) thermal-hydraulic solution (in the presence of nuclear heat load), (b) hydraulic solution [3] (in the absence of nuclear heat load). Each plot includes both a map of the vertical component of the flow velocity on a poloidal cross section (colour scale on the right), and the streamlines (coloured according to the colour scale on the left, based on the velocity magnitude). (For interpretation of the references to colour in this figure legend, the reader is referred to the web version of this article.)

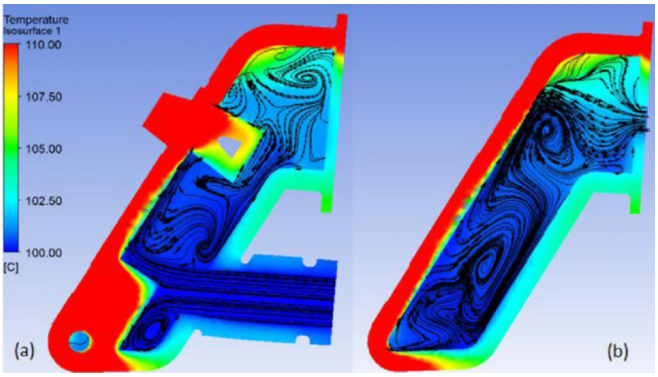

Fig. 21. Temperature maps on different poloidal cross sections in the TrS: (a) across an inlet hole; (b) across an outlet hole. The flow field is also reported. The temperature is not clipped to its largest value, i.e., the values larger than 110 °C are represented equal to 110 °C.

(wall) temperature T_S of those structures, and of a suitable (local) bulk temperature T_B of the coolant.

While q'' and T_S can be extracted from the computed solution, in the situation at hand, where the fluid flow is completely 3D, the identification of T_B is very hard. We then choose to compute the HTC with reference to the inlet temperature T_{in} as

$$HTC = \frac{q''}{T_S - T_{in}} \leq HTC_{def} \quad (1)$$

which is a conservative choice since everywhere in the VV the fluid temperature will be larger than the inlet temperature.

Wall heat flux: Fig. 22 shows the map of the wall heat flux computed in the OB segment. The region with the highest heat flux is concentrated around the housings, especially those in the first two rows below the equatorial ports, where the peak heat load is located, see Fig. 8a.

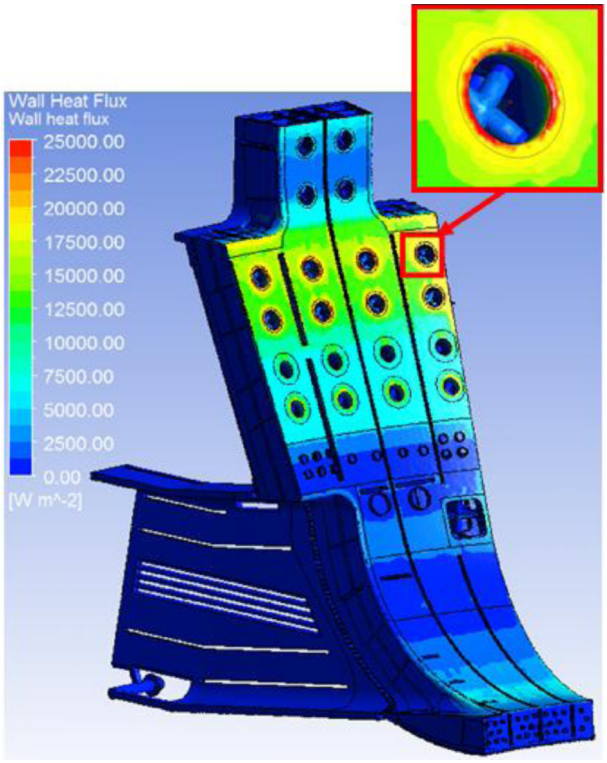

Fig. 22. Wall heat flux on the OB, view from the plasma side. In the inset: zoom around and inside one of the housings, with water pipes.

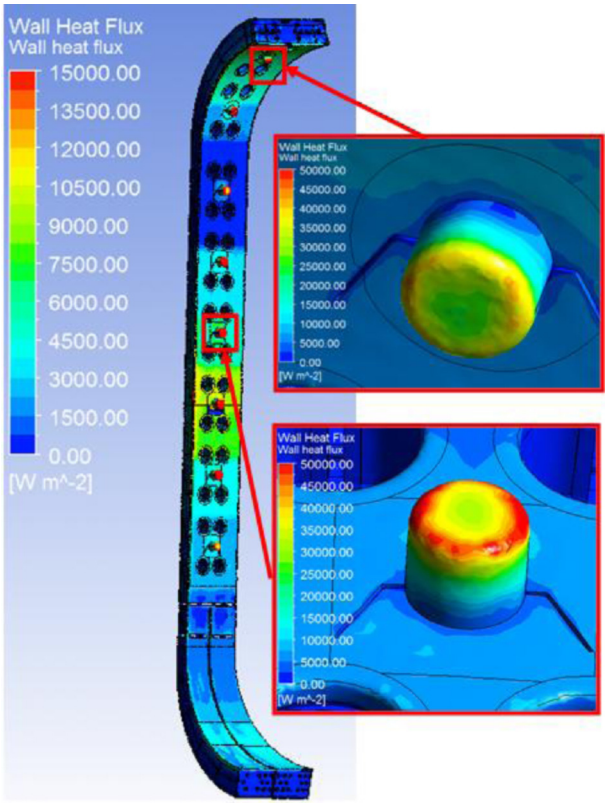

Fig. 23. Wall heat flux on the Inb, view from the plasma side. In the insets: zooms on the fluid surface in the IMK #4 and #8.

Fig. 23 reports the wall heat flux computed in the Inb segment. The regions with the highest heat flux are concentrated here at the IMKs, where the highest temperature on the VV surface in this segment is reached, see Fig. 13. Note that the inner shell around the IMK #6 is subject to a very low level of heat flux, which will lead to very small HTC values estimated in this region, see below.

The peak values of the wall heat flux are computed in the OT segment, see Fig. 24, in view of the needs to remove the highest nuclear load of the entire VV, see Figs. 7 and 8b. The region where the wall heat flux reaches its maximum is located again around the housings, and especially that on the upper port frame, see also above.

Wall temperature: In Fig. 25 the wall temperature computed for the OB segment is shown. The effect of the flow field on the temperature field can be appreciated by the slightly higher temper-ature (worst cooling) corresponding to the regions where a smaller coolant flow rate is present, see for instance the top part of the side poloidal channels (solid circle region in Fig. 25), or where the flow is re-circulated back from the Inb, see [3] and the dashed circle region in Fig. 25. In the OB, the wall hot spot is at ~125 °C and is located below the frame of the equatorial port, where again a less efficient cooling has been computed.

The wall temperature computed for the Inb is shown in Fig. 26. The hot spot is at ~140 °C and is located below the head of the most loaded IMK #4.

The wall temperature distribution computed for the OT is reported in Fig. 27, including a zoom on the hot spot below the housings located on the upper port frame. However, the relatively coarse mesh in the hot spot region could affect the accuracy of the computed maximum wall temperature in this segment.

The maximum wall temperature computed on the sector (~140 °C) is well below the saturation temperature (~175 °C at 0.9 MPa) of the water coolant at the operating pressure,

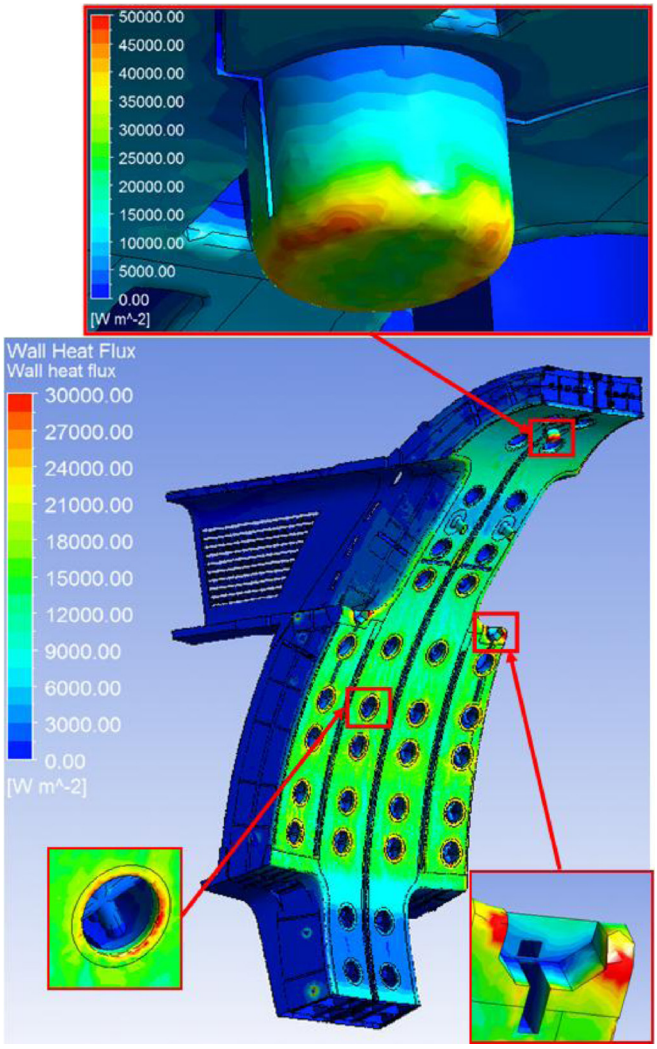

Fig. 24. Wall heat flux in the OT, view from the plasma side. In the insets: zooms on the fluid surface around some of the housings.

guaranteeing that the latter remains in the single-phase state of sub-cooled liquid.

Heat transfer coefficient: In previous work [8], it was estimated that, in order to keep the thermal stress of the VV below the allowable, a high heat removal capability, such as a heat transfer coefficient of 500 W/m^2 K on the wall surfaces, was required for the VV cooling. In this section, we discuss to what extent this target on the HTC is confirmed to be achieved by the present detailed thermal-hydraulic analysis.

The computed *HTC* maps are reported below for the different segments. For each segment we use two different scales: one up to 2000 W/m^2 K, for the overall picture, and the other up to 500 W/m^2 K, to highlight the critical regions from the point of view of the *HTC*.

In the OB segment, the largest portion of the wetted surfaces presents *HTC* values much larger than 500 W/m^2 K, up to ~2000 W/m^2 K. Fig. 28 shows the HTC maps computed on different surfaces in the OB, where all HTC values above 500 W/m^2 K are represented as equal to 500 W/m^2 K. It is seen that only few spots with an *HTC* < 500 W/m^2 K are found on the inner shell, while large regions with very small *HTC* are computed on the outer shell. However, the heat load on the outer shell is small enough to avoid any concern on the cooling. On the IWS, some regions present a small

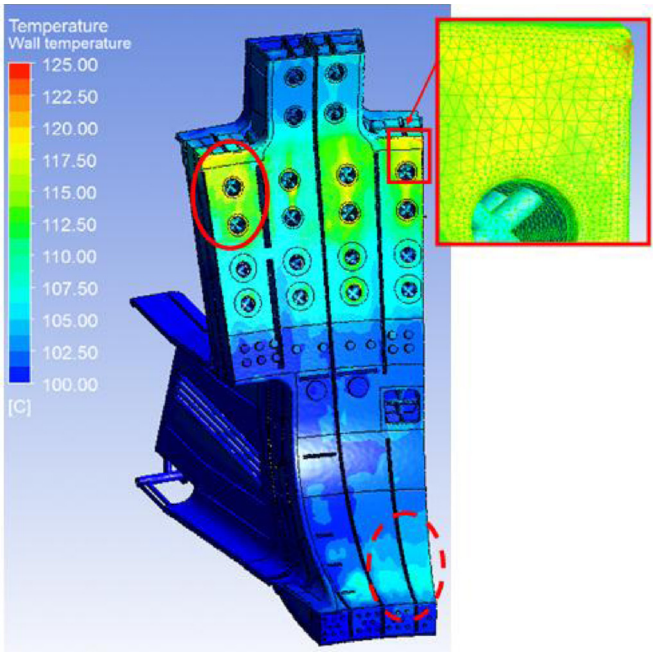

Fig. 25. Wall temperature map computed in the OB, view from the plasma side. In the inset: zoom on the hot spot location on the frame of the lateral equatorial port (the surface grid is also shown). Solid and dashed ovals indicate regions where a smaller coolant flow rate is present.

HTC, but there only a relatively small nuclear heat load is present, as already mentioned.

In the Inb segment, the largest portion of the wetted surfaces presents *HTC* values much larger than 500 W/m^2 K. In particular, the heavily loaded heads of the IMKs are characterized by 1000 < *HTC* < 2000, see Fig. 29. The most critical region of the Inb inner shell (and of the facing IWS as well), from the point of view of the HTC, appears to be the one around the IMK #6, see Fig. 29.

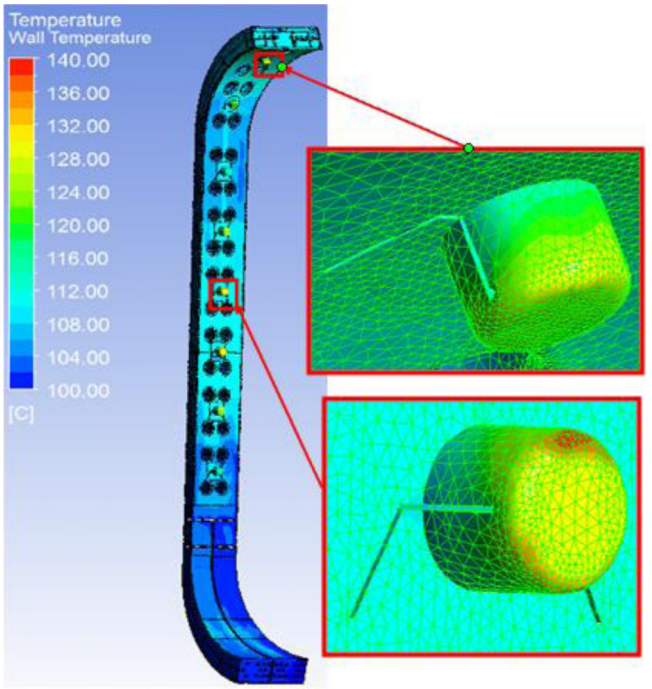

Fig. 26. Wall temperature map computed in the Inb, view from the plasma side. In the insets: zoom on the hot spots (the surface grid is also reported).

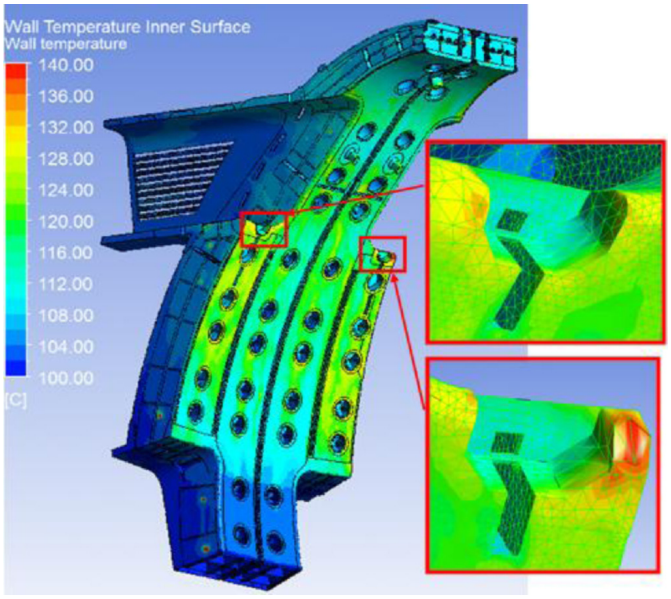

Fig. 27. Wall temperature map computed in the OT, view from the plasma side. In the insets: zoom on the hot spot locations on the frame of the lateral equatorial port.

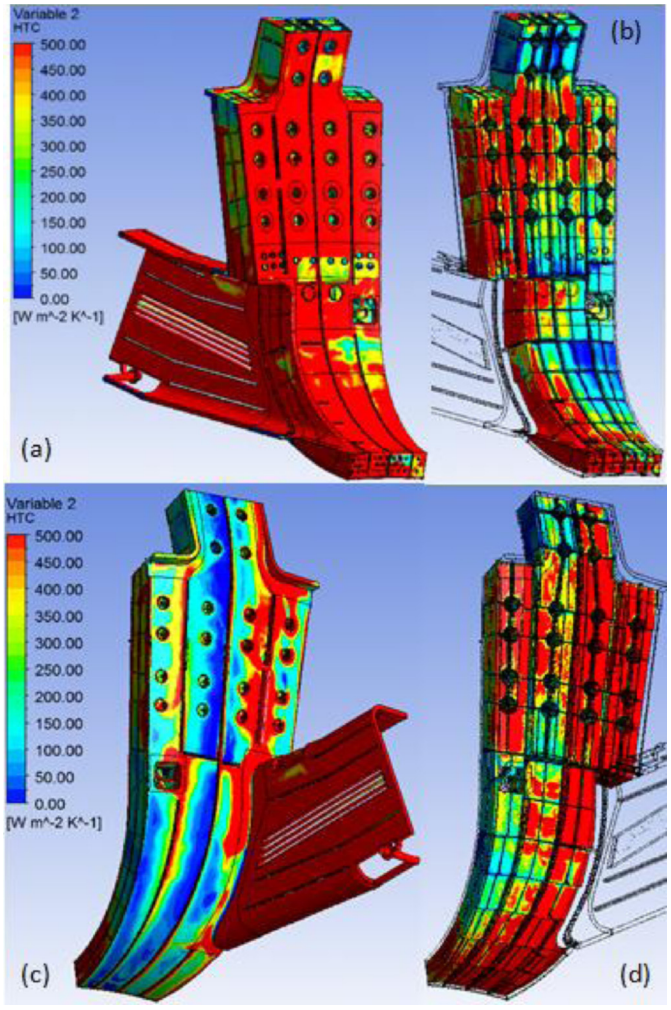

Fig. 28. Map of the *HTC* on different surfaces of the OB segment, plotted on a scale up to 500 W/m^2 K: (a) inner side of the inner shell; (b) IWS surface facing the inner shell; (c) inner side of the outer shell; and (d) IWS surface facing the outer shell. No clipping was applied, i.e., all HTC values above 500 W/m^2 K are represented as equal to 500 W/m^2 K in the figure.

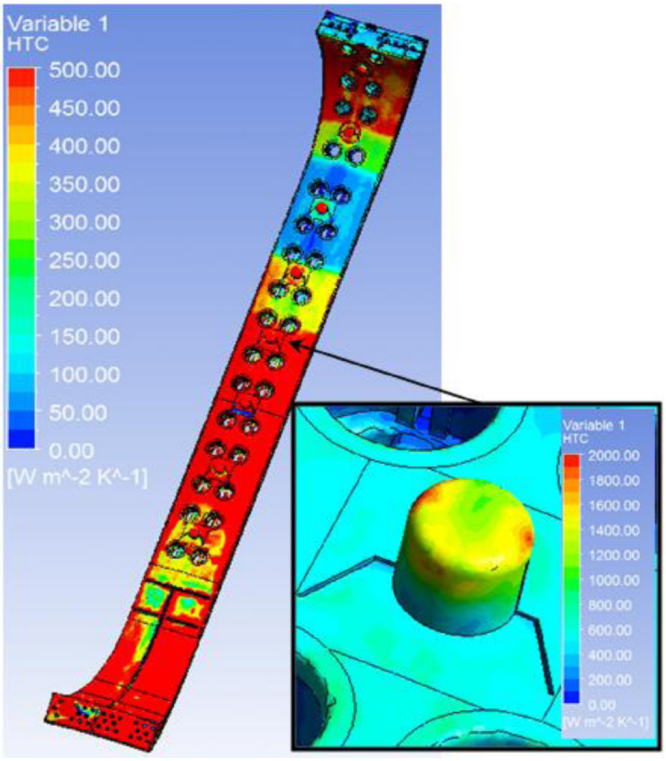

Fig. 29. Map of the *HTC* on the inner side of the inner shell plotted on a scale up to 500 W/m^2 K (all HTC values above 500 W/m^2 K are represented as equal to 500 W/m^2 K). In the inset the map on the surface of the fluid domain of the IMK # 4 is shown.

However, the low *HTC* computed there can be an artefact of the choice $T_B = T_{in}$. Indeed, while the nuclear heat load is low at that location, see Fig. 8c, the temperature difference $T_S - T_{in}$ is not correspondingly small. The Inb outer shell presents almost everywhere an *HTC* below the limit, not shown, but this again should not be a concern, in view of the very low heat load on the outer shell.

For the OT segment, see Fig. 30, similar considerations apply as for the Inb.

The computed HTC in the TrS (not shown) is almost everywhere safely larger than 500 W/m^2 K.

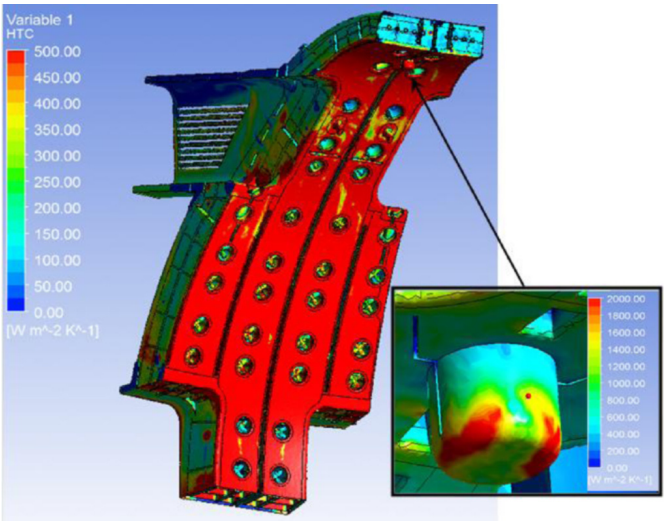

Fig. 30. Map of the *HTC* on the inner side of the inner shell plotted on a scale up to 500 W/m^2 K (all HTC values above 500 W/m^2 K are represented as equal to 500 W/m^2 K); inset: IMK # 9.

8. Conclusions

In this Part II, the Computational Fluid Dynamics study of Part I has been used as the basis for the steady-state analysis of the thermal-hydraulic effects of the recently reassessed nuclear heat load on the regular sector #5 of the ITER vacuum vessel.

Important details of the VV structure, like housings and inter-modular keys, have been included for the first time in the computational model of the sector. However, in view of the significant computational cost (~90 million cells needed for an adequate discretization of the complete geometry of the half sector), we have separately solved the conjugate heat transfer problem in each segment (inboard, outboard bottom and top, triangular support), then coupled them iteratively and finally performed a global consistency check to confirm the accuracy of the procedure for the whole sector.

The major results of the present thermal-hydraulic analysis are as follows:

- The hot spots on the structures are at ~290 °C in the two housings on the upper port frame and at ~230 °C in the most loaded inter-modular key.
- The temperature of the wetted surfaces is well below the coolant saturation temperature.
- The heat transfer coefficient in the portions of the sector subject to the highest nuclear heat load is typically above the 500 W/m^2 K target.

Acknowledgement

The work at Politecnico di Torino was partially financially supported by F4E under contract F4E-2009-OPE-031-01-01. The views and opinions expressed herein do not necessarily reflect those of the ITER Organization.

Appendix A. Numerics

This Appendix describes a few numerical features of the mesh generation and of the solution process.

A.1. Mesh quality

The similar issues as discussed in [3] were encountered in the generation of the mesh for the thermal-hydraulic problem considered here, with the obvious additional complication of having to mesh now also the solid components with their complex geometry.

The features of our final mesh, obtained again after several smoothing steps, are summarized in Table 2, with particular reference to the worst cells. As to the cell equiangle skew parameter, FLUENT recommends that no cells are above 0.95, while concerning the orthogonal quality ortho parameter the FLUENT recommendation is that no cells are below 0.01. By comparison with the FLUENT recommendations, we consider our final mesh acceptable.

Table 2
Conservation errors.

Segment	% of cells with "skew" < 0.05	% of cells with "ortho" < 0.05
OB	0.025	0.014
Inb	0.001	0.002
OT	0.004	0.010

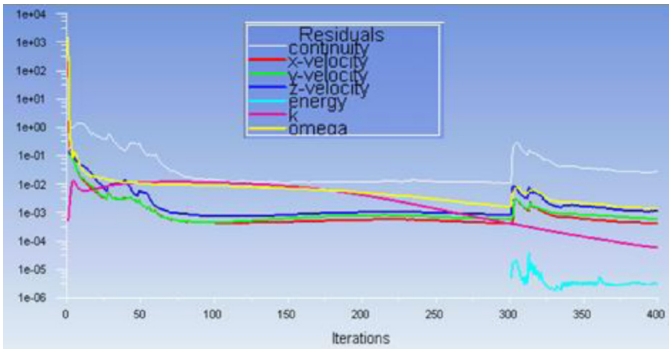

Fig. 31. Residual history in the thermal-hydraulic simulation of the Inb segment.

Table 3
Distribution of mesh quality parameters.

Segment	Relative error on mass conservation (%)	Relative error on energy conservation (%)
OB	0.0013	1.8
Inb	1.3×10^{-6}	2.1
OT	0.11	3.2
TrS	8.7×10^{-6}	6.5

A.2. Convergence to steady state

A detailed study of the effect of the smoothing of the mesh on the computed solution has been performed in an ad-hoc initially isothermal case without heat load. The results on the original mesh (without smoothing) were compared with the results on the mesh obtained after 15 smoothing steps. In the case without smoothing the residual of the energy equation starts increasing. On the contrary, in the case after 15 mesh smoothing steps, this increase is not

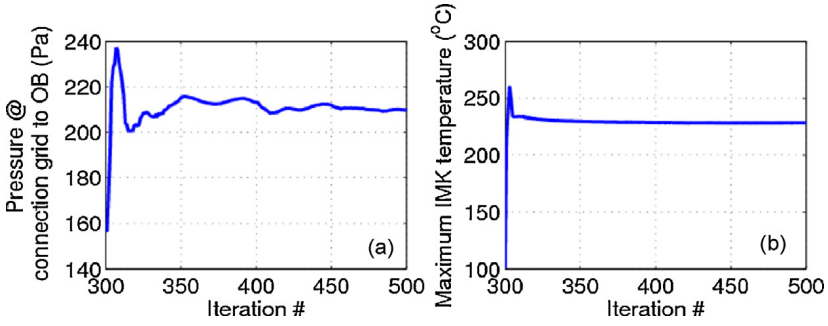

Fig. 32. Monitor history in the Inb simulation: (a) average pressure at the connection grid to the OB; and (b) maximum temperature in the IMKs.

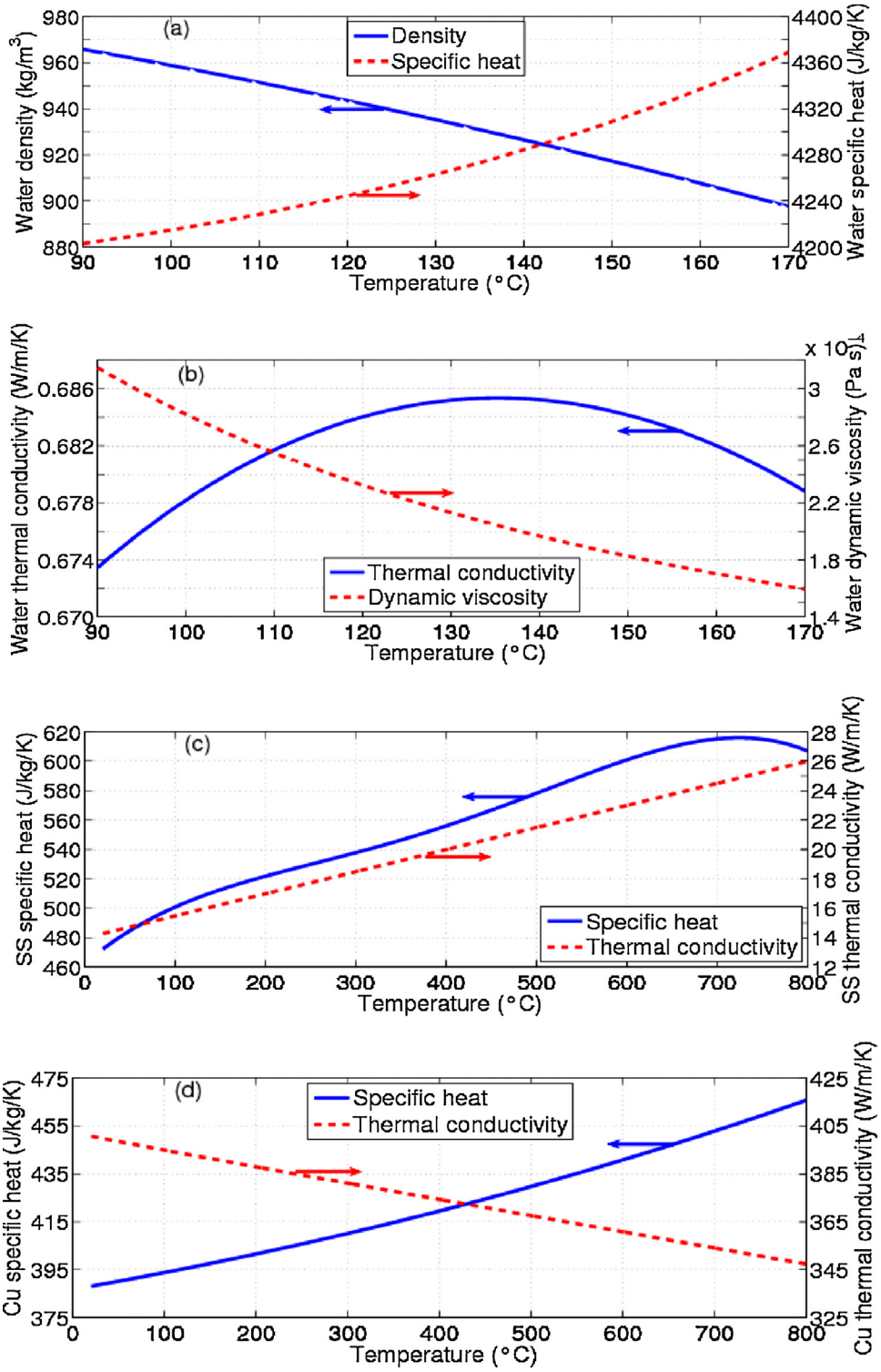

Fig. 33. Temperature dependence of selected material properties: (a) and (b), water coolant; (c) SS; and (d) Cu.

only delayed but also constrained to acceptable values.[1] We adopt this condition of a limited increase of the energy residual (and of the associated number of cells "with problems") over a relatively large number of iterations, as the practical definition of an acceptably converged steady-state solution.

In the actual case with nuclear heat load, we first look for a steady flow field in each segment, and then we switch the energy equation on. The history of the residuals as the iterations proceeds in the solution of the thermal-hydraulic problem for the Inb segment is shown in Fig. 31. In this particular case, the steady flow field

[1] As an example, while after 75 iterations the number N_{drift} of cells where the temperature is drifting away from the initial guess is ~10 (i.e., less than one in a million) on both the original and the 15 times smoothed mesh, after 150 iterations N_{drift} ~ 3000 on the original mesh, but only ~30 on the mesh obtained after 15 smoothing steps.

Table 4
Results of mesh independence study (structures).

	Mass flow rate = 40 kg/s			Mass flow rate = 4 kg/s		
# tetrahedra/10^6 (solid domain)	ΔT_{max}^{shell} (°C)	ΔT_{max}^{IWS} (°C)	ΔT_{out} (°C)	ΔT_{max}^{shell} (°C)	ΔT_{max}^{IWS} (°C)	ΔT_{out} (°C)
0.277[a]	**114.41**[a]	**2.07**[a]	**0.064**[a]	**137.67**[a]	**4.83**[a]	**601**[a]
0.305	114.34	2.07	0.064	137.20	4.76	600
4.96	113.94	2.06	0.064	136.53	4.63	603

[a] This row in boldface corresponds to the mesh with the same parameters as used in the present paper for the entire half sector.

is reached after ~300 iterations and the energy residual appears in the plot only after that.

In Fig. 32 field we show the corresponding history of two monitors. It is seen that the solution can be considered to have reached a steady state with a good level of accuracy.

The final check on the quality of the steady state obtained in each segment is based on the verification of mass and energy conservation. It is seen in Table 3 that in each segment the conservation error in the computed solution is at most of few percent, which we consider quite good for our purpose.

A.3. Mesh independence study

As for the hydraulic analysis presented in [3], also the mesh independence of the thermal-hydraulic solutions presented here has been verified considering the same simple domain as in [3].

In this case, the simulations have been performed assuming a uniform heat load of 200 kW/m^3 in the shells (fully representative of the nuclear load on the VV), and 50 kW/m^3 in the IWS.

The results reported in Table 4, in terms of maximum temperature increase in the shells and in the IWS, as well as of average fluid outlet temperature, confirm that the mesh selected for the present analysis is adequate.

Appendix B. Material properties

This appendix presents in the form of the plots below the variation over the relevant temperature range of the thermo-physical properties of the materials, which are relevant for the present simulations (Fig. 33).

References

[1] K. Ioki, C.H. Choi, E. Daly, S. Dani, J. Davis, B. Giraud, et al., ITER vacuum vessel design and construction, Fus. Eng. Des. 87 (2012) 828–835.
[2] K. Ioki, A. Bayon, C.H. Choi, E. Daly, S. Dani, J. Davis, et al., Progress of ITER vacuum vessel, Fus. Eng. Des. (2013) (in press).
[3] L. Savoldi Richard, R. Bonifetto, R. Zanino, S. Corpino, G. Obiols-Rabasa, J. Izquierdo, et al., CFD analysis of a regular sector of the ITER vacuum vessel. Part I: flow distribution and pressure drop, Fus. Eng. Des. (2013) (accepted for publication).
[4] D.-H. Kim, S. Cho, H.-J. Ahn, K.-H. Park, G.-W. Hong, Y.-H. Choi, et al., Detailed design of ITER vacuum vessel ports and in-wall shielding, J. Korean Phys. Soc. 49 (December) (2006) S345–S349.
[5] S. Cho, D.-H. Kim, S.-I. Pak, H.-J. Ahn, K.-H. Park, Y.-K. Kim, et al., Current status of ITER vacuum vessel design activities in Korea, J. Korean Phys. Soc. 49 (December) (2006) S437–S441.
[6] www.cfd-online.com/Wiki/SST_k-omega_model
[7] SAS IP, Inc., ANSYS ICEM CFD Help Manual, version 14.5, 2012.
[8] M. Onozuka, K. Ioki, G. Sannazzaro, Y. Utin, H. Yoshimura, Design and thermal/hydraulic characteristics of the ITER-FEAT vacuum vessel, Fus. Eng. Des. 58–59 (2001) 857–861.
[9] Water properties, IAPWS IF-97 by Magnus Holmgren, www.x-eng.com
[10] SAS IP, Inc., ANSYS FLUENT Help Guide, version 13.0, 2010.